J. Fluid Mech. (1993), vol. 246, pp. 465–488

Three-dimensional flow over two spheres placed side by side

By INCHUL KIM, SAID ELGHOBASHI AND WILLIAM A. SIRIGNANO

Department of Mechanical and Aerospace Engineering, University of California, Irvine, CA 92717, USA

(Received 23 August 1991 and in revised form 28 July 1992)

Three-dimensional flow over two identical (solid or liquid) spheres which are held fixed relative to each other with the line connecting their centres normal to a uniform stream is investigated numerically at Reynolds numbers 50, 100, and 150. We consider the lift, moment, and drag coefficients on the spheres and investigate their dependence on the distance between the two spheres. The computations show that, for a given Reynolds number, the two spheres are repelled when the spacing is of the order of the diameter but are weakly attracted at intermediate separation distances. For small spacing, the vortical structure of the near wake is significantly different from that of the axisymmetric wake that establishes at large separations. The partially confined flow passing between the two spheres entrains the flows coming around their other sides. Our results agree with available experimental and numerical data.

1. Introduction

Flows past droplets and solid particles are important in many natural and engineering applications such as air pollution, combustion systems, and chemical processes. Many investigations have considered the interactions between droplets or particles and the surrounding fluid by analytical and numerical methods. For sufficiently low or high Reynolds numbers, a theoretical analysis can be performed using singular perturbation expansions which involve linearization or the boundary-layer approximation. For flows at intermediate Reynolds numbers, which are most common in engineering applications, it is necessary to solve the Navier–Stokes equations numerically.

The majority of the published numerical studies for intermediate Reynolds numbers have focused on flows past a single particle and are thus relevant only at low particle concentration. In regions of large concentration, the drag coefficient is significantly different from that of an isolated particle at the same Reynolds number, and the lift and moment (torque) coefficients have finite values. In order to understand the behaviour of a particle in a large-concentration region, studies of the interactions amongst particles are required. Unfortunately, in practice, the spacial arrangement of particles or droplets in a region of large concentration is quite complex and subject to uncertainty, and calculations involving the entire region are at present not feasible. In order to develop statistical approaches, information about individual droplet or particle interactions is needed.

The study of droplet or particle arrays, particularly in flows at intermediate Reynolds number, is relatively new (Patnaik 1986). A particle array as discussed by

Sirignano (1983) consists of a few particles in a well-defined geometrical arrangement or a large number of particles in a periodic configuration. These arrays, although artificial, can provide information on particle–particle interactions and their effects on the ambient conditions in the vicinity of the particle. The simplification in the geometry allows a detailed and rigorous analysis.

Tal, Lee & Sirignano (1983) studied the hydrodynamics and heat transfer in assemblages of solid spheres in a steady flow at Reynolds number 100 (based on the particle diameter and relative velocity). Their method took advantage of the periodic nature of an infinite array of spheres. They considered several spheres in tandem, and found a trend of decreasing drag coefficients in the streamwise direction. Tal, Lee & Sirignano (1984) also studied the interaction of two solid spheres in tandem in a steady uniform flow at $Re = 40$ for two different spacings using bispherical coordinates and indicated that the drag coefficient of either sphere is always less than that of a single isolated sphere and that the reduction is much greater for the downstream sphere.

Patnaik (1986) investigated the interaction of two vaporizing droplets in tandem at $Re = 50$ and 100 for interdroplet spacing equal to 4.25 diameters using the downstream solution of the lead droplet as the inflow conditions for the downstream droplet. He found that for both Reynolds numbers, the drag coefficient of the trailing droplet is lower than that of the leading droplet.

Raju & Sirignano (1990) studied the interactions between two moving vaporizing droplets in tandem at $50 \leqslant Re \leqslant 200$ for a range of spacings and droplet radii ratios. They found that the drag coefficients for both droplets are less than that of a solid sphere and, for the same Reynolds number, the trailing droplet has lower drag. Chiang & Sirignano (1992*a*, *b*) extended this study to include variable properties and two and three droplets. With three droplets, the difference in drag coefficients between the second and third droplets is much smaller than for the first and second droplets.

All of the above studies employed axisymmetric calculations. Recently, some numerical studies have been performed for three-dimensional flows over a *single* solid sphere. Dandy & Dwyer (1989) obtained three-dimensional numerical solutions for steady, uniform shear flow past a fixed, heated spherical particle over a range of Reynolds numbers ($0.1 \leqslant Re \leqslant 100$) and dimensionless shear rates ($0.005 \leqslant \alpha \leqslant 0.4$). They found that at a fixed shear rate, the lift coefficient is approximately constant over a wide range of intermediate Reynolds numbers, and the drag coefficient also remains constant when normalized by the drag for a sphere in uniform flow. Tomboulides, Orszag & Karniadakis (1991) performed a numerical study of three-dimensional flow past a sphere using a spectral element method for $30 \leqslant Re \leqslant 1000$ and discussed steady axisymmetric states and unsteady states with three-dimensional vortex shedding.

Three-dimensional flow interactions between droplets or particles at finite Reynolds number have not yet been studied. As a first step towards understanding the three-dimensional interactions in large concentration of particles, we investigate flow interactions between two identical (solid or liquid) spheres which are held fixed side by side against the uniform stream at Reynolds numbers 50, 100, and 150. We determine the effects of three-dimensional interactions on the lift, moment, and drag coefficients as a function of the dimensionless distance between the two spheres and Reynolds number. Some novel phenomena in the near wake are discovered as the gap between the two spheres decreases. Our results are also compared with available experimental and numerical data.

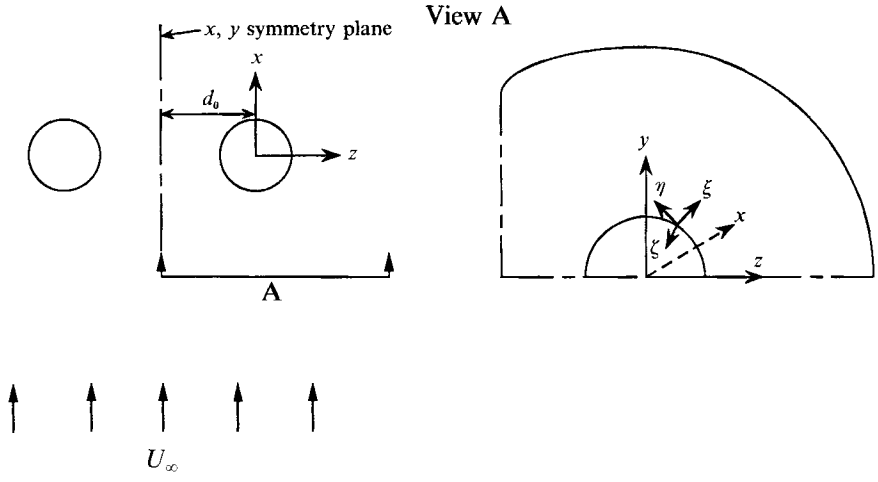

FIGURE 1. Flow geometry and coordinates.

2. Problem statement and numerical solution

We consider a steady three-dimensional incompressible laminar flow of a Newtonian fluid past two identical (solid or liquid) spheres held fixed, with the line connecting the sphere centres normal to a uniform stream, as shown in figure 1; d_0 denotes the distance, normalized by the sphere radius, from the sphere centre to the x, y symmetry plane between the two spheres. Far upstream, the flow is uniform with constant velocity $U_\infty \boldsymbol{i}$ parallel to the x-axis. Two symmetry planes are noted in figure 1: the (x, z)-plane containing the centres of the two spheres and the (x, y)-plane located at $z = -d_0$ midway between the sphere centres.

We note that asymmetry of the flow past neighbouring bluff bodies might occur at lower Reynolds number than that of the first temporal instability for a single body. An example is the flow past two cylinders where flow asymmetry would occur well before the first temporal instability for a single cylinder. In contrast, we expect that, for the flow past two spheres, flow asymmetry would occur nearly simultaneously with the temporal instability since the interaction between the two halves (each containing one sphere) of the flow field should be stronger for cylinders than for spheres. That is, the flow between the two spheres is less constrained than the flow between the two side-by-side cylinders.

Two coordinate systems are used in our formulation: the Cartesian coordinates (x, y, z) and the non-orthogonal generalized coordinates (ξ, η, ζ). The origin of the former coincides with the sphere centre; and ξ is the radial, η the angular, and ζ the azimuthal coordinate. Owing to symmetry, the physical domain is reduced to one quarter of an ellipsoid-like space.

The domain of the external flow is bounded by $1 \leqslant \xi \leqslant N_1$, $1 \leqslant \eta \leqslant N_2$, $1 \leqslant \zeta \leqslant N_3$, where $\xi = 1$ and N_1 correspond, respectively, to the sphere surface and the far-field boundary surrounding the sphere; $\eta = 1$ and N_2 denote, respectively, the positive z-axis and the negative z-axis; $\zeta = 1$ and N_3 refer, respectively, to the (x, z)-plane in the positive x-direction and the (x, z)-plane in the negative x-direction.

The domain of the internal flow is $1 \leqslant \xi_l \leqslant N_{1l}$, $1 \leqslant \eta_l \leqslant N_2$, $1 \leqslant \zeta_l \leqslant N_3$. $\xi_l = 1$ and N_{1l} correspond to the centre and the surface of the sphere, respectively. $\eta_l = 1$ and N_2 denote the positive z-axis and the negative z-axis, respectively. $\zeta_l = 1$ and N_3 refer to the (x, z)-plane in the positive x-direction and the (x, z)-plane in the negative

x-direction, respectively. Within the liquid sphere, ξ_l = constant are a family of concentric spherical surfaces. Uniform spacing ($\delta\xi = \delta\eta = \delta\zeta = 1$) is used, for convenience, for the generalized coordinates in both flows.

The non-orthogonal generalized coordinate system of the external flow can be easily adapted to three-dimensional arbitrary geometries. We solve the continuity equation and the time-dependent Navier–Stokes equations and relax them to the steady-state solution, as will be discussed in detail in §2.2.

2.1. *Governing equations and boundary conditions*

Since one of our goals is to study the flow interaction with liquid spheres, we present the equations for the flows inside and outside the spheres. However, for flow interactions with solid spheres, only the external flow equations are solved. The continuity and momentum equations inside and outside a sphere and the boundary conditions are non-dimensionalized using the sphere radius a_0 as the characteristic length and U_∞ as the characteristic velocity:

external flow

$$\nabla \cdot \boldsymbol{V} = 0, \tag{1}$$

$$\frac{\mathrm{D}\boldsymbol{V}}{\mathrm{D}t} = -\nabla p + \frac{2}{Re}\nabla^2 \boldsymbol{V}; \tag{2}$$

internal flow

$$\nabla \cdot \boldsymbol{V}_l = 0, \tag{3}$$

$$\frac{\mathrm{D}\boldsymbol{V}_l}{\mathrm{D}t} = -\nabla p_l + \frac{2}{Re_l}\nabla^2 \boldsymbol{V}_l. \tag{4}$$

The governing equations are written with respect to the generalized coordinates (ξ, η, ζ), which allows a three-dimensional body of arbitrary shape to be treated. The numerical integration is performed using a cubic computational mesh with equal spacing ($\delta\xi = \delta\eta = \delta\zeta = 1$) (Anderson, Tannehill & Pletcher 1984).

The conditions at the interface, $\xi = 1$ or $\xi_l = N_{1l}$, are derived by requiring continuity of the shear stresses and tangential velocities. Because no fluid is allowed to cross the surface of the liquid sphere, the normal velocities at the interface are zero in both flows. An interface condition for the pressure is obtained from the momentum equation. Since the interface is always spherical, it is more convenient to cast these conditions in terms of spherical coordinates (r, θ, ϕ):

$$\tau_{r\theta,s} = \tau_{l,r\theta,s}, \tag{5}$$

$$\tau_{r\phi,s} = \tau_{l,r\phi,s}, \tag{6}$$

$$V_{\theta,s} = V_{l,\theta,s}, \tag{7}$$

$$V_{\phi,s} = V_{l,\phi,s}, \tag{8}$$

$$V_{r,s} = V_{l,r,s} = 0, \tag{9}$$

$$\frac{\partial p}{\partial r_{,s}} = V_{\theta,s}^2 + V_{\phi,s}^2 + \frac{2}{Re}\left[\frac{\partial}{\partial r}\left(r^2\frac{\partial V_r}{\partial r}\right) - 2\frac{\partial V_\theta}{\partial \theta} - 2V_\theta \cot\theta - \frac{2}{\sin\theta}\frac{\partial V_\phi}{\partial \phi}\right]_{,s}, \tag{10}$$

where the subscript s denotes the surface of the liquid sphere. For the solid-sphere case, the no-slip condition is enforced on the sphere surface.

The external flow boundary conditions are:

$$p = 0, \quad u = 1, \quad v = 0, \quad w = 0 \quad \text{at} \quad \xi = N_1 \text{ except at } z = -d_0, \tag{11}$$

$$\frac{\partial p}{\partial z} = \frac{\partial u}{\partial z} = \frac{\partial v}{\partial z} = 0, \quad w = 0 \quad \text{at} \quad z = -d_0, \tag{12}$$

$$\frac{\partial p}{\partial \eta} = \frac{\partial u}{\partial \eta} = \frac{\partial w}{\partial \eta} = 0, \quad v = 0 \quad \text{at} \quad \eta = 1 \quad \text{and} \quad N_2, \tag{13}$$

$$\frac{\partial p}{\partial \zeta} = \frac{\partial u}{\partial \zeta} = \frac{\partial w}{\partial \zeta} = 0, \quad v = 0 \quad \text{at} \quad \zeta = 1 \quad \text{and} \quad N_3, \tag{14}$$

where u, v, and w are the velocities of the external flow in the x-, y-, and z-directions, respectively. p is the pressure, and the subscript l denotes the internal flow. Equations (12) and (14) correspond, respectively, to the symmetry conditions in the x, y symmetry plane between the spheres and the x, z symmetry plane containing the centres of the spheres. Equation (13) expresses the no-flux boundary condition for p, u, and w on the axes $\eta = 1$ and $\eta = N_2$, and zero v-velocity in the x, z symmetry plane containing the two axes.

The internal flow boundary conditions are

$$\frac{\partial p_l}{\partial \xi_l} = \frac{\partial u_l}{\partial \xi_l} = \frac{\partial w_l}{\partial \xi_l} = 0, \quad v_l = 0 \quad \text{at} \quad \xi_l = 1, \tag{15}$$

$$\frac{\partial p_l}{\partial \eta_l} = \frac{\partial u_l}{\partial \eta_l} = \frac{\partial w_l}{\partial \eta_l} = 0, \quad v_l = 0 \quad \text{at} \quad \eta_l = 1 \quad \text{and} \quad N_2, \tag{16}$$

$$\frac{\partial p_l}{\partial \zeta_l} = \frac{\partial u_l}{\partial \zeta_l} = \frac{\partial w_l}{\partial \zeta_l} = 0, \quad v_l = 0 \quad \text{at} \quad \zeta_l = 1 \quad \text{and} \quad N_3, \tag{17}$$

where (15) and (16) correspond, respectively, to the no-flux boundary conditions at the centre of the droplet and on the axes $\eta_l = 1$ and N_2, and zero v_l-velocity in the x, z symmetry plane containing the two axes. Equation (17) prescribes the symmetry condition on the x, z symmetry plane containing the centres of the spheres.

The dimensional drag, lift, and moment coefficients are evaluated from

$$F_D = \int_S -p\boldsymbol{n}\cdot\boldsymbol{i}\,\mathrm{d}S + \int_S \boldsymbol{n}\cdot\boldsymbol{\tau}\cdot\boldsymbol{i}\,\mathrm{d}S, \tag{18}$$

$$F_L = \int_S -p\boldsymbol{n}\cdot\boldsymbol{k}\,\mathrm{d}S + \int_S \boldsymbol{n}\cdot\boldsymbol{\tau}\cdot\boldsymbol{k}\,\mathrm{d}S, \tag{19}$$

$$M = \int_S \boldsymbol{r}\times\boldsymbol{\tau}\,\mathrm{d}S, \tag{20}$$

where S denotes the surface of the sphere, $\boldsymbol{n}$ is the outward unit normal vector at the surface, $\boldsymbol{r}$ is the position vector from the centre of the sphere, and $\boldsymbol{\tau}$ is the viscous stress tensor. Equations (18)–(20) are evaluated on the side of the external flow. The lift force is assumed positive when it is directed toward the positive z-axis. Owing to symmetry, only the y-component of the moment is non-zero and is assumed positive in the counter-clockwise direction.

Non-dimensional coefficients of drag, lift, and moment are defined respectively as

$$C_D = F_D/(\tfrac{1}{2}\rho U_\infty^2 \pi a_0^2), \tag{21}$$

$$C_L = F_L/(\tfrac{1}{2}\rho U_\infty^2 \pi a_0^2), \tag{22}$$

$$C_M = \boldsymbol{M}\cdot\boldsymbol{j}/(\tfrac{1}{2}\rho U_\infty^2 \pi a_0^3). \tag{23}$$

2.2. *Numerical solution*

We have developed a three-dimensional implicit finite-difference algorithm to solve simultaneously the set of discretized partial differential equations. The method is based on an Alternating-Direction-Predictor-Corrector (ADPC) scheme to solve the time-dependent Navier–Stokes equations. ADPC is a slight variation of Alternating-Direction-Implicit (ADI) method. It is first-order accurate in time but is effective and implemented easily when embedded in a large iteration scheme (Patnaik 1986). The control volume formulation is used to develop the finite-difference equations from the governing equations with respect to the generalized coordinates (ξ, η, ζ). One of the advantages of the control volume formulation is that all dependent variables are conserved over a single control volume, and hence the whole domain regardless of the grid fineness. An important part of solving the Navier–Stokes equations in primitive variables is the calculation of the pressure field. In the present work, a pressure correction equation is employed to satisfy indirectly the continuity equation (Anderson *et al.* 1984). The pressure correction equation is of the Poisson type and is solved by the Successive-Over-Relaxation (SOR) method.

The overall solution procedure is based on a cyclic series of guess-and-correct operations. The velocity components are first calculated from the momentum equations using the ADPC method, where the pressure field at the previous time step is employed. This estimate improves as the overall iteration continues. The pressure correction is calculated from the pressure correction equation using the SOR method, and new estimates for pressure and velocities are obtained. This process continues until the solution converges at each time step. For the flow past liquid spheres, the same procedure is performed in the flow inside the sphere. The governing equations of motion in each flow are solved in an interactive sequence through the interface boundary conditions until convergence is achieved for each time step of the calculation.

The generation of the computational grid for the external multi-sphere flows is an essential part of the solution procedure. We generate the three-dimensional grid efficiently by choosing the outer boundary of the physical domain to be axisymmetric about the line connecting the centres of the two spheres and constructing an axisymmetric grid. The axisymmetric grid is generated on the (ξ, η)-plane including the line that connects the centres of the two spheres and by using a hybrid method of algebraic and differential equation methods. First, we choose the outer boundary of the computational grid as the x, y symmetry plane and an incomplete ellipse whose centre is located at the centre of the sphere, as shown in figure 1. We then generate a family of quarter-ellipses on the right side of the domain, another family of quarter-ellipses on the left side, and also a family of straight lines emanating from the centre of the sphere. Grid density is controlled by the stretching function developed by Vinokur (1983). This is followed by solving the quasi-linear elliptic system of differential equations using the SOR method with a few (not more than two) iterations in order to smooth the grid lines generated by the algebraic method. In figures 2 (*a–c*), we present a cross-section of the three-dimensional grid at $d_0 = 21$, 10, and 3.

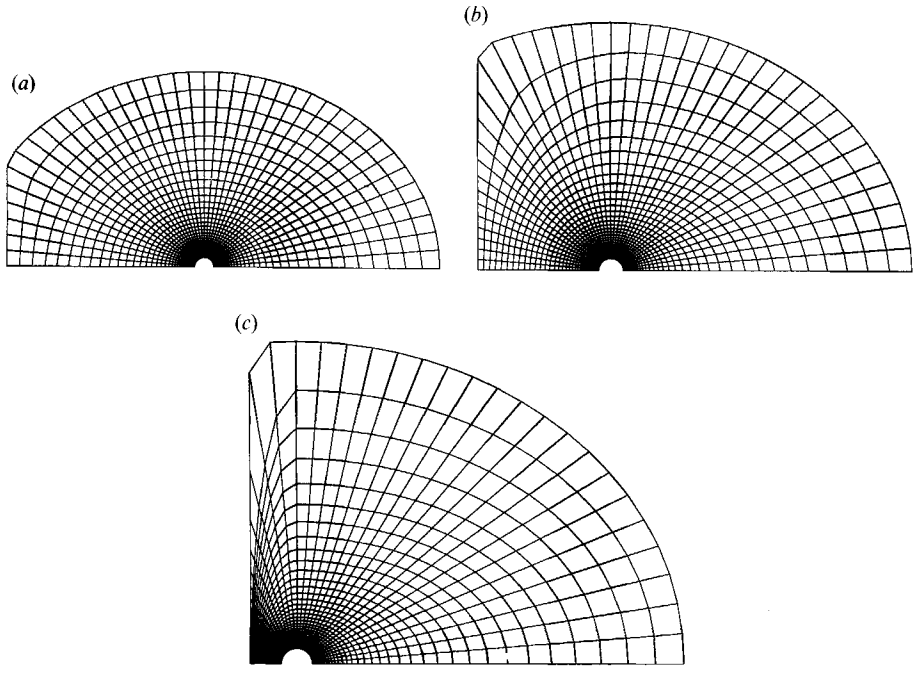

FIGURE 2. Cross-section of the three-dimensional grid system for (*a*) $d_0 = 21$; (*b*) $d_0 = 10$; (*c*) $d_0 = 3$.

$N_1 \times N_2 \times N_3$	C_{DP}	C_{DV}	C_D	C_D^*
$Re = 50$				
$20 \times 21 \times 21$	0.706	0.951	1.657	
$30 \times 31 \times 31$	0.683	0.934	1.617	
$40 \times 41 \times 41$	0.676	0.929	1.605	1.58
$Re = 100$				
$20 \times 21 \times 21$	0.555	0.593	1.148	
$30 \times 31 \times 31$	0.532	0.582	1.114	
$40 \times 41 \times 41$	0.524	0.581	1.105	1.09

TABLE 1. Drag coefficients as a function of grid density at $Re = 50$ and 100 where * denotes the data from Roos & Willmarth (1971) and also Clift *et al.* (1978).

3. Results and discussion

In §3.1, we test the accuracy of the full three-dimensional solution procedure by predicting the axisymmetric flow over a single (solid and liquid) sphere. In §3.2, we discuss the three-dimensional interactions between two solid spheres, and in §3.3, we examine the three-dimensional interactions between two liquid spheres.

3.1. *Flow over a single sphere*

We discuss the flow generated by an impulsively started solid sphere in a quiescent fluid at two Reynolds numbers: 50 and 100. The time-dependent solution converges asymptotically to a steady state, which is in excellent agreement with available experimental data and correlations as shown in tables 1 and 2. Table 1 lists the drag coefficients as a function of the computational grid density at Reynolds numbers 50

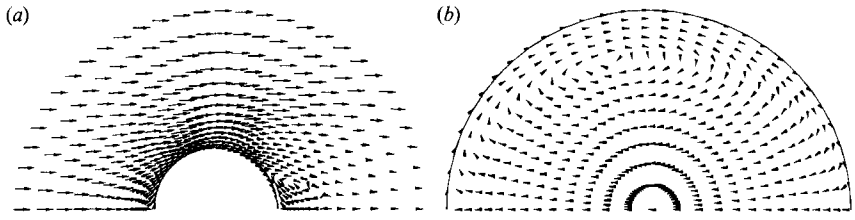

FIGURE 3. Velocity vector fields of (*a*) external flow; (*b*) internal flow for the axisymmetric flow past a liquid sphere at $Re = 50$.

$N_1 \times N_2 \times N_3$	P_{0f}	P_{0r}	θ_s	θ_s^*
$Re = 50$				
$20 \times 21 \times 21$	0.611	−0.1088	136.53	
$30 \times 31 \times 31$	0.606	−0.0982	138.10	
$40 \times 41 \times 41$	0.604	−0.0954	138.63	139.3
$Re = 100$				
$20 \times 21 \times 21$	0.555	−0.0924	124.24	
$30 \times 31 \times 31$	0.555	−0.0819	125.74	
$40 \times 41 \times 41$	0.554	−0.0789	126.25	126.5

TABLE 2. Pressure at the front and rear stagnation points and the separation angle measured from the front stagnation point as a function of grid density at $Re = 50$ and 100, where * denotes the data from Taneda (1956) and Clift *et al.* (1978).

and 100 respectively, and compares them with the data of Roos & Willmarth (1971) and also with the correlations of Clift, Grace & Weber (1978). Table 2 shows the pressures at the front and rear stagnation points and the separation angle measured from the front stagnation point as a function of grid density at Reynolds number 50 and 100, in comparison with the data of Taneda (1956) and also with the correlations of Clift *et al.* (1978). Although the solution in these test cases are axisymmetric, none of the three velocity components in our formulation becomes identically zero. Therefore, the three-dimensional solution scheme is fully exercised here. The calculations were performed for three different grids, $(N_1 \times N_2 \times N_3) = (20 \times 21 \times 21)$, $(30 \times 31 \times 31)$, and $(40 \times 41 \times 41)$, in a computational domain with an outer boundary located at 21 sphere radii from the sphere centre. The dimensionless times needed to reach steady state for Reynolds number 50 and 100 are 9 and 15, respectively.

We tested the solution procedure by varying the far-field boundary condition and by changing the location of the outer boundary. In the first test, the far-field outflow boundary condition was changed from a free-stream condition to $\mathrm{D}\phi/\mathrm{D}t = 0$ ($\phi = u$, v, or w). There was a little difference in the results for the velocity field in the far wake just near the outer boundary, but almost no difference in the drag coefficient and the near-wake size (the separation angle and length of the recirculation eddy) at Reynolds numbers 50 and 100. In the second test, the location of the outer boundary was changed from 21 to 33 sphere radii. There was about 1 % difference in the length of the recirculation eddy, but virtually no change in the drag coefficient and the separation angle of recirculation eddy at both Reynolds numbers. This indicates that, even though the boundary condition given by (11) does not allow for a momentum defect in the far wake, the error is just local, and the near-field solution is only weakly affected.

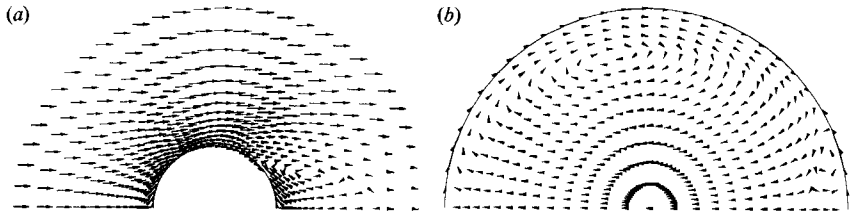

FIGURE 4. Velocity vector fields of (*a*) external flow; (*b*) internal flow for the axisymmetric flow past a liquid sphere at $Re = 100$.

The axisymmetric test-run for a solid sphere at Reynolds number 100 with the $40 \times 41 \times 41$ grid required a dimensionless time step of $\Delta t = 0.002$ and a total time of 3.75 Cray Y-MP/8-64 cpu hours. Each time step takes about 1.8 cpu seconds.

We also solved the flow generated by an impulsively started liquid sphere in a quiescent fluid, and the results were in good agreement with available numerical studies. Figure 3 (*a*, *b*) shows the steady-state velocity vector distributions of the flow past a liquid sphere with viscosity ratio of 25 and density ratio of 300 (internal to external fluid) at Reynolds number 50. We observe a closed-streamline wake detached from the liquid sphere, and thus no secondary recirculating flow is found in the liquid phase (Rivkind & Ryskin 1976; Clift *et al.* 1978). In figure 4 (*a*, *b*) we show the velocity vector distributions for the same parameters as above except that the Reynolds number is 100. It is interesting to note that a second circulatory flow develops in the liquid-sphere stern region. This behaviour was observed in an earlier study by Rivkind & Ryskin (1976) where a stream function–vorticity formulation was employed. Rivkind & Ryskin (1976) indicated that when the density ratio is much greater than the viscosity ratio, i.e. the Reynolds number inside the liquid sphere is much greater than the Reynolds number outside, a second circulatory flow possibly occurs in the liquid-sphere stern region. The axisymmetric test run for the liquid sphere required half the time step for the solid sphere and was about 3.4 times slower because of the numerical interaction between the internal and external flows.

For the interactions between two spheres, an ellipsoid-like domain is chosen in order to take into account the interactions when the two spheres are far away from each other. As shown in figure 1, a longer outer boundary $r_\infty = 25$ is chosen in the z-direction, and $r_\infty = 21$ is chosen in the σ-direction, where $\sigma = (x^2+y^2)^{\frac{1}{2}}$. The results using the above ellipsoid outer boundary for a single sphere were identical in the steady axisymmetric flow calculations to those using the spherical outer boundary.

The results of the $30 \times 31 \times 31$ grid differ by only 0.8% in the drag coefficients and 0.4% in the separation angles from those of the $40 \times 41 \times 41$ grid as shown in tables 1 and 2. The percentage difference was calculated as follows. Let the result of the $30 \times 31 \times 31$ grid be S_1 and the result of the $40 \times 41 \times 41$ grid be S_2. Then, the percentage difference is $(S_1 - S_2)/S_1$. Thus, we chose the medium-size grid $30 \times 31 \times 31$, and $15 \times 31 \times 31$ inside the liquid sphere, for the following calculations. A typical run for the solid sphere with the $30 \times 31 \times 31$ grid required 0.8 cpu hours on the Cray Y-MP/8-64; the liquid sphere run with the same grid required 2.7 cpu hours. 15 runs were made for each Reynolds number to cover the range of $1.5 \leqslant d_0 \leqslant 25$.

We did not perform calculations for Reynolds number higher than 150, because it is known that the wake becomes unstable at a Reynolds number in the range of 130–220 for a single sphere (Taneda 1956; Goldburg & Florsheim 1966; Roos & Willmarth 1971; Nakamura 1976; Kim & Pearlstein 1990) and our present goal is to

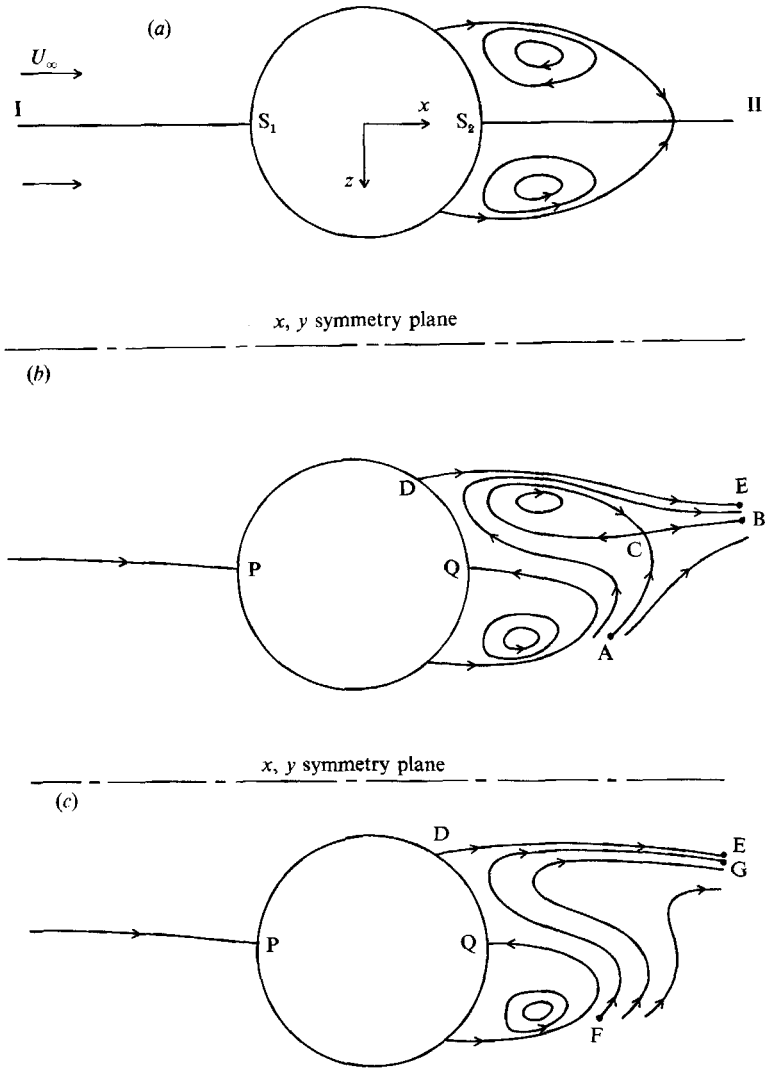

FIGURE 5. Sketch of typical streamlines over one of the two solid spheres in the principal plane (x, z-plane) at $Re = 100$ for (a) axisymmetric flow; (b) $d_0 = 2$; (c) $d_0 = 1.5$.

obtain steady-state solutions. For the solution of a flow including the three-dimensional unsteady wake, a complete computational domain (i.e. encompassing the two spheres without a symmetry plane) and periodic boundary conditions in ζ-direction will be necessary.

3.2. *Interactions of two solid spheres*

3.2.1. *Flow structure*

In order to illustrate better the fluid motion, we consider the flow field in the (x, z)-plane of symmetry, which is defined as the *principal plane*, where the narrowest path between the two spheres occurs, hence the strongest interactions between them.

Figure 5 (a) displays a sketch of the actual streamlines around a single sphere in the principal plane at Reynolds number 100. As expected, two identical counter-rotating vortices (corresponding to a single vortex ring) exist in the wake, and the

downstream stagnation point is located on the axis of symmetry. Line I–II connecting the front and rear stagnation points in the standard axisymmetric flow over a single sphere will be used as a reference line: we refer to the region above this line as the 'top' or 'upper' region and that below as the 'bottom' or 'lower' region.

Figure 5(*b*) displays a sketch of the actual streamlines around one of the two spheres in the principal plane at Reynolds number 100. The two spheres are separated by a distance $d_0 = 2$. Owing to the *blockage* of the flow in the gap between the two spheres, the streamlines diverge away from the x, y symmetry plane (located at $z = -d_0$) as they approach the front stagnation region. Thus, the stagnation streamline of the single-sphere case (I–S_1 in figure 5*a*) no longer intersects the sphere, and another streamline closer to the symmetry plane meets the sphere to form the new front stagnation streamline at point P. As a consequence, the fluid particles move faster in the lower left region around the sphere than in the upper left region, and this causes the pressure in the lower left region to be lower than that in the upper left region. The resulting pressure difference between the upper and lower left regions is higher than that between the bottom of the sphere and the narrow path. This pressure imbalance, which will be discussed in §3.2.2, causes repulsion of the two spheres. The contribution of shear stress differences to the repulsion will also be discussed in §3.2.2.

Figure 5(*b*) shows an interesting streamline pattern in the wake region. Two counter-rotating eddies exist in the wake but their configuration is quite different from that for axisymmetric flow. The lower eddy is formed by the fluid separating on the lower portion of the sphere as in the case of axisymmetric flow. The upper eddy is not formed by the fluid separating on the upper portion of the sphere, but rather by the fluid turning around the lower eddy and being entrained by the upper flow. This upper eddy is detached from the sphere. A portion of the fluid moving around the bottom of the sphere passes between the detached upper eddy and the sphere. The streamline A–B encompassing the upper eddy intersects itself, and the intersection point, C, designated as the downstream stagnation point, is shifted toward the x, y symmetry plane. Both eddies are smaller than those of the axisymmetric flow. These new features can be explained as follows. The pressure above the upper wake is less than that below the lower wake owing to the increased acceleration of the fluid in the narrow path between the two spheres (as will be shown in figure 7). Thus, the fluid particles turning around the lower eddy are pushed into the upper region of the wake. The pressure distribution around the sphere will be discussed further in §3.2.2.

Figure 5(*c*) shows a sketch of the actual streamline pattern at Reynolds number 100 for the case $d_0 = 1.5$. The shifting of the front stagnation streamline and stagnation point toward the x, y symmetry plane is more obvious here than in the previous case of $d_0 = 2$. The significant difference is in the wake region where both the upper eddy and downstream stagnation point vanish. Fluid particles separating on the upper portion of the sphere move downstream without returning (streamline D–E). On the other hand, fluid particles turning around the lower eddy move into the upper region of the wake until they reach near the upper separation point, D, and then move downstream in an S-shaped path (streamline F–G) without returning to form an eddy. The lower eddy shrinks as the two spheres become closer, and the pressure difference between the top and bottom of the wake is larger.

It is interesting to examine the changes in the separation region at the sphere surface for the cases $d_0 = 2$ and 1.5. More specifically, we examined the behaviour of the circle of intersection of the wake and the sphere. Our results show that the circle

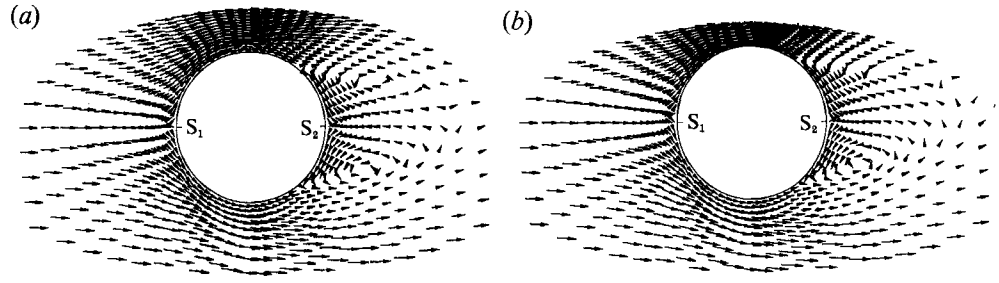

FIGURE 6. Velocity vector fields over one of the two solid spheres in the principal plane corresponding to (*a*) figure 5(*b*), $d_0 = 2$; (*b*) figure 5(*c*), $d_0 = 1.5$.

is slightly shifted toward the x, y symmetry plane due to the decreased pressure in the gap region with respect to that in the wake lower region. This shifting produces separation angles at the top, middle, and bottom of the sphere with values of 123.1°, 126.5°, and 126.2° respectively for the case $d_0 = 1.5$, where the angles are measured from the front stagnation point of the axisymmetric flow case. This is in contrast with an angle of 125.7° at all positions for a single sphere.

Figure 6(*a*) shows the computed velocity vector field corresponding to figure 5(*b*), $d_0 = 2$. The velocity vectors upstream of the front stagnation point, S_1, for axisymmetric flow point downwards away from the x, y symmetry plane. This indicates that the front stagnation point (P in figure 5*b*), is shifted toward the x, y symmetry plane. Similar behaviour occurs at the rear stagnation point (Q in figure 5*b*). Figure 6(*b*) shows the computed velocity vector field corresponding to figure 5(*c*), $d_0 = 1.5$.

One of the advantages of the velocity vector plot is that it shows clearly the relative magnitude of velocity in the flow field, e.g. the smaller velocity in the wake region compared to that outside the wake is seen in figure 6(*a*, *b*). However, it is difficult to obtain streamlines directly from the tangents of the velocity vector plot.

A stream function ψ cannot be defined and calculated from the velocity in the principal plane owing to the existence of a divergence associated with the third component of velocity. Nevertheless, for descriptive purposes only, it is convenient to use the algorithm

$$\psi_{\rm ps}(r, \theta_0) = \psi_{\rm ps}(r_0, \theta_0) + \int_{r_0}^{r} -u_\theta \, {\rm d}r \tag{24}$$

to present approximations to the streamline pattern. It is understood that since a true stream function does not exist, the pseudo-stream function is dependent upon the integration path. The above algorithm specifically involves only radial integration; u_θ can be recovered by differentiation of this function, but u_r cannot be recovered. The streamlines presented in figures 5(*a–c*) were based on this algorithm.

Phenomena in the wake similar to those described above have been found in a few previous studies. Rosfjord (1974) obtained results similar to those in figures 5(*b*) and 5(*c*) in his experimental and numerical studies of the recirculating flow region between two-dimensional parallel separated jets. He found that for velocity ratios between two jets equal to 1.11 and 1.25 (upper to lower), two eddies exist near the injector face, but the upper eddy is detached from the injector face, and a portion of the fluid originating at the lower jet is entrained by the upper jet, passing between the detached upper eddy and the injector face. He also reported that for a velocity ratio of 1.4, only the lower eddy existed and a complete entrainment of the weaker

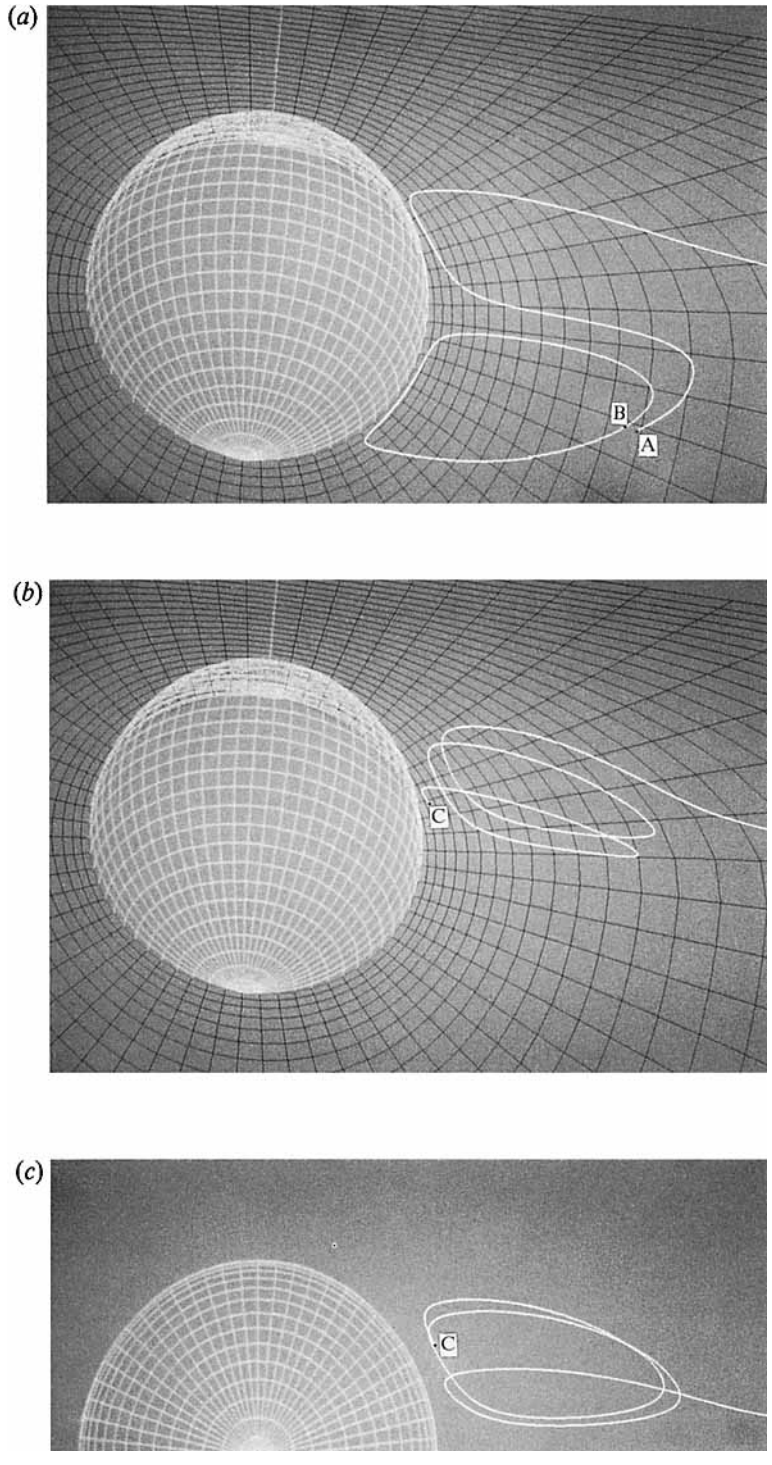

FIGURE 7. (*a*) Pathlines of two fluid particles (A and B) slightly above the principal plane ($y = 0.001$) of the two solid spheres. (*b*, *c*) Pathline of a fluid particle (C) whose initial position was ($x, y, z = 0.995, 0.575, 0$): (*b*) a view from top of the sphere looking toward the x, y symmetry plane; (*c*) a side view looking normal to the x, y symmetry plane.

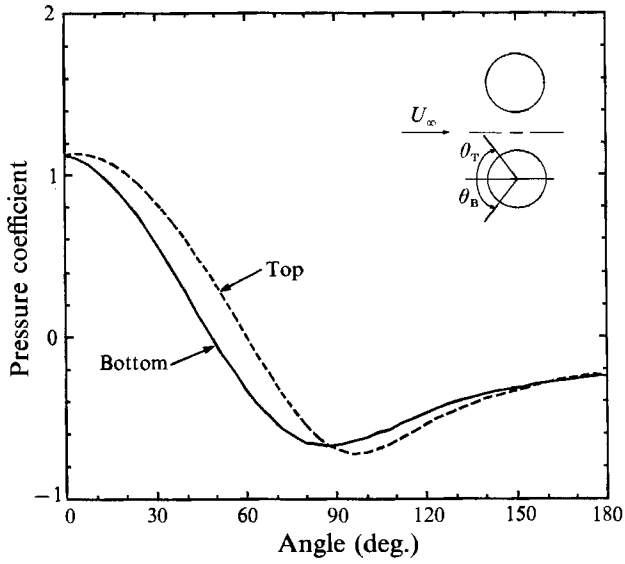

FIGURE 8. Distribution of the pressure coefficient around the solid sphere in the principal plane at $Re = 100$ for $d_0 = 1.5$.

jet was observed. In particular, the flow S-shaped loop near the stronger jet was clearly indicated. Recently, Dandy & Dwyer (1990) also found a flow pattern similar to figure 6(*b*) in their numerical study of steady uniform shear flow past a single solid sphere.

In order to facilitate the visualization of the three-dimensional character of the flow in the wake region discussed above, we present the pathlines of selected fluid particles in figure 7(*a–c*), at Reynolds number 100 for $d_0 = 2$, where the free-stream direction is from left to right. The pathlines $\boldsymbol{x}(x_0, y_0, z_0, t)$, where the subscript 0 denotes initial particle location, were obtained by solving three coupled ordinary differential equations $\mathrm{d}\boldsymbol{x}/\mathrm{d}t = \boldsymbol{u}(\boldsymbol{x})$, via a fourth-order Runge–Kutta method.

We first selected two fluid particles (A and B) slightly above the principal plane ($y = 0.001$) separated by a small distance (much smaller than the sphere radius) in the wake region. Figure 7(*a*) shows that particle A follows an S-shaped pathline. On the other hand, particle B follows a closed-loop pathline as was discussed in the previous section.

We then examined the pathline of a fluid particle C whose initial position (x_0, y_0, $z_0 = 0.995, 0.575, 0$) was in the wake region but above the principal plane. Figure 7(*b*) (a view from top of the sphere looking toward the x, y symmetry plane) shows that the fluid particle C first follows a helical pathline as it approaches the x, y symmetry plane and then moves downstream. Figure 7(*c*) is a side view (looking normal to the x, y symmetry plane) of that pathline.

3.2.2. *Pressure and shear stress distribution*

Figure 8 shows the pressure coefficient, $2(p - p_\infty)/\rho U_\infty^2$, around one of the spheres in the principal plane at Reynolds number 100 for $d_0 = 1.5$. On average, the pressure is higher on the top, contributing to a positive lift force. The pressure on the bottom of the sphere is lower between 0° and 87.6° and also slightly lower between 159° and 180° in the wake region than that on the top of the sphere, where the angle is measured from the front stagnation point ($\theta = 0$) of the axisymmetric flow case. On

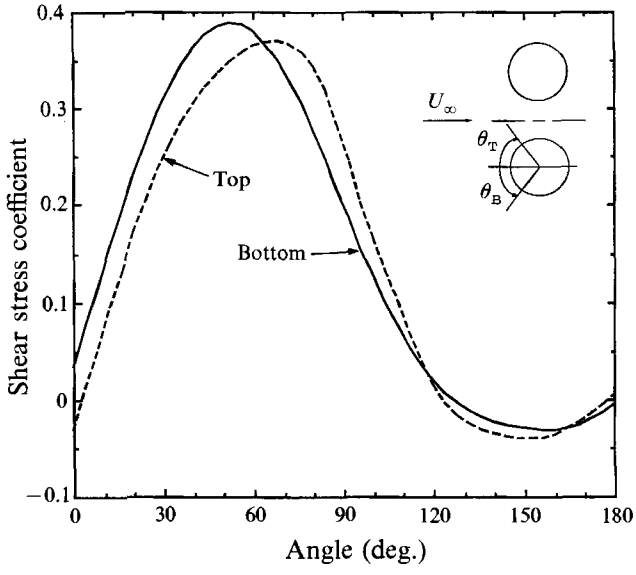

FIGURE 9. Distribution of shear stress coefficient around the solid sphere in the principal plane at $Re = 100$ for $d_0 = 1.5$.

the bottom of the sphere, the minimum pressure occurs at an angle less than 90°. On the top of the sphere, the minimum pressure occurs at an angle greater than 90° and is lower than the minimum pressure on the bottom of the sphere. The maximum pressure occurs a few degrees toward the x, y symmetry plane measured from $\theta = 0$. The highest pressure in the wake region occurs a few degrees toward the x, y symmetry plane measured from $\theta = \pi$. These observations indicate that the front and rear stagnation points are shifted a few degrees toward the x, y symmetry plane.

Figure 9 shows the tangential shear stress coefficient, $2\tau_{r\theta}/\rho U_\infty^2$, in the same plane used for the pressure coefficient in figure 8. Note that the clockwise direction is considered positive for the shear stress on the top of the sphere, and the counterclockwise direction is considered positive for the shear stress on the bottom. It is seen that the shear stress, on average, is higher around the lower part of the sphere than around the top. In particular, the magnitude of the shear stress is higher in the lower regions $\theta = 0$ to 63.6 and $\theta = 165.5$ to π than on the top of the sphere. It is also important to note that, owing to their inclinations with the x-axis, the shear forces on these two lower regions contribute to both the lift (parallel to the z-axis) and drag (parallel to the x-axis), whereas the shear force at the top of the sphere contributes mainly to the drag. Thus, the shear forces in this case contribute, along with the pressure forces, to the repulsion of the two spheres. The shear stress at $\theta = 0$ is not zero but acts counterclockwise, and the shear stress at $\theta = \pi$ is not zero but acts clockwise. Therefore, the front and rear stagnation points are shifted a few degrees toward the x, y symmetry plane. Another interesting feature is that the separation angle where the shear stress vanishes on the top of the sphere is 123.1°, but that angle on the bottom is 126.2°. The computed separation angle of 125.7° for the axisymmetric flow case with the medium-size grid was shown in table 2. Thus, the reverse flow in the wake region is shifted upwards toward the x, y symmetry plane.

We examine next the tangential velocity profiles, $u_\theta(r)$, at two different θ-locations on the bottom and top of the sphere in the principal plane at Reynolds number 100

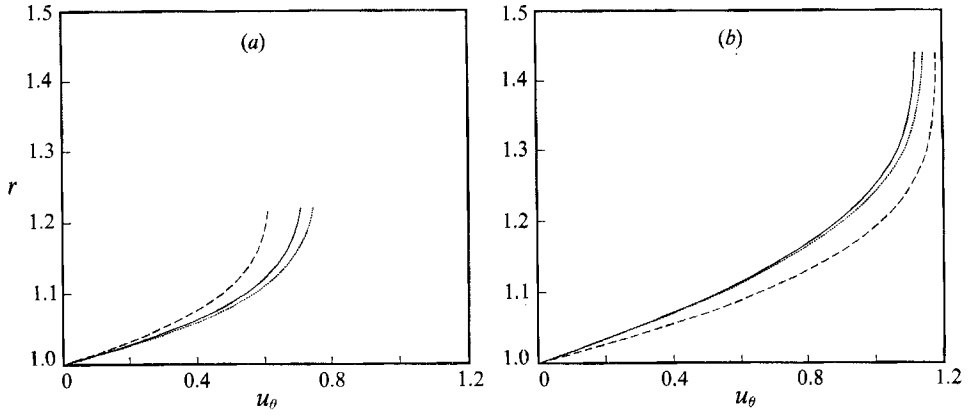

FIGURE 10. Tangential velocity profile on the bottom and top of the solid sphere in the principal plane at (*a*) $\theta = 36°$; (*b*) $\theta = 84°$: ——, single sphere; · · · · · ·, bottom; – – –, top.

for $d_0 = 1.5$. Figure 10(*a*) shows the tangential velocity profiles at $\theta = 36°$ on the bottom and top of one of the spheres, in addition to that for the axisymmetric case as a reference. It is seen that the maximum velocity at the bottom is higher than at the top, as mentioned earlier in the discussion of figure 5(*b*). It is also seen that the velocity gradient at the sphere surface is higher at the bottom than at the top, hence the higher shear stress at the bottom as explained earlier (see figure 9). Figure 10(*b*) shows the tangential velocity profiles at $\theta = 84°$ on the bottom and top of the sphere, in addition to that for the axisymmetric case. It is seen that now the velocity gradient at the top wall is 26% higher than at the bottom although the maximum velocity at the top is only 3% higher than the maximum value at the bottom. The reason is that the boundary-layer growth at the top is limited by the interaction with the boundary layer of the other sphere.

3.2.3. *Lift coefficients*

In the following discussion, we classify the proximity of the two spheres into three regimes: *close*, *intermediate*, and *far separated*, depending on the values of d_0 and Reynolds number.

Figure 11(*a–c*) show the total lift coefficient and the lift coefficients due to viscous and pressure contributions, respectively, as a function of d_0 at Reynolds numbers 50, 100, and 150. The total lift coefficient, figure 11(*a*), is positive when the two spheres are close ($d_0 < 7.9$ for $Re = 50$, $d_0 < 4$ for $Re = 100$, and $d_0 < 3.4$ for $Re = 150$). That is, the two spheres repel each other, and the repulsion is stronger the closer they are. Our results show that both the viscous and pressure contributions have an important effect on the repelling force, but the pressure contribution is more dominant when $Re \geqslant 100$ (compare figure 11*b*,*c*). On the other hand, the total lift coefficient is negative and relatively small – that is, the two spheres attract each other weakly – at intermediate separation distances ($7.9 < d_0 < 21$ for $Re = 50$, $4 < d_0 < 21$ for $Re = 100$, and $3.4 < d_0 < 21$ for $Re = 150$). At these distances, the pressure is the main contributor to the attraction force at all Reynolds numbers. The smaller the Reynolds number is, the smaller the pressure effect, the weaker the attraction, and the narrower the region of attraction. When $d_0 \geqslant 21$, however, the lift vanishes, and the two spheres have no interactions at any Reynolds numbers.

As discussed in §3.2.1, when the two spheres are in close proximity, the front stagnation point is shifted toward the x, y symmetry plane, and the fluid particles

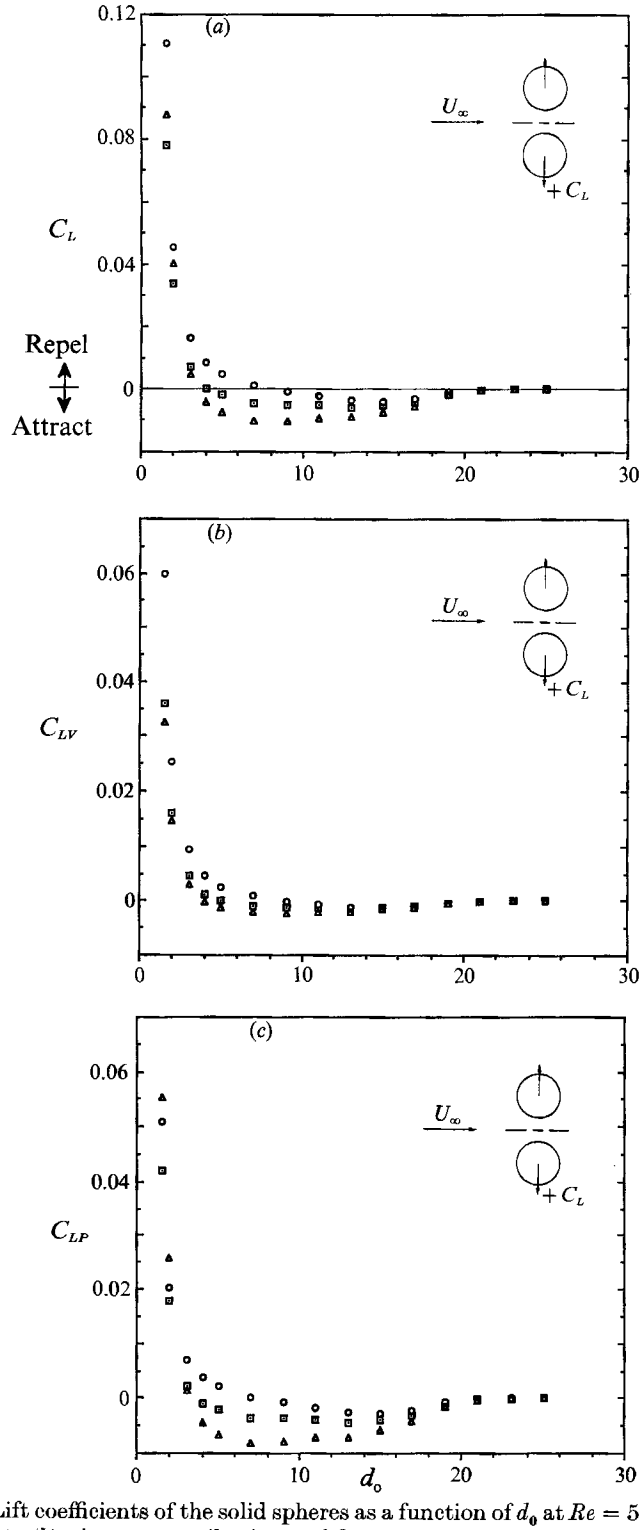

FIGURE 11. Lift coefficients of the solid spheres as a function of d_0 at $Re = 50$, 100, and 150: (*a*) total lift coefficient; (*b*) viscous contribution to lift; (*c*) pressure contribution to lift. ○, $Re = 50$; ⊡, $Re = 100$; △, $Re = 150$.

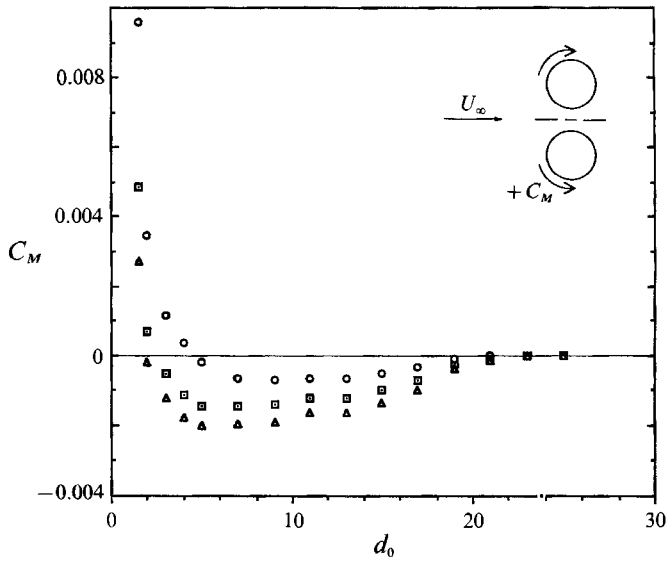

FIGURE 12. Moment coefficient of the solid spheres as a function of d_0 at $Re = 50$, 100, and 150. Symbols as figure 11.

accelerate faster in the lower left region than in the upper left region of the sphere. This difference in acceleration results in a net negative pressure gradient normal to and away from the x,y symmetry plane, contributing to the repulsion between the two spheres. The shear stress is also higher in the lower left region than in the upper left as shown in figure 9. Furthermore, owing to its inclination with the x-axis, the shear force in the lower left region contributes to both the lift (parallel to the z-axis) and drag (parallel to the x-axis), whereas the shear force at the top of the sphere contributes mainly to the drag. Therefore, both the pressure and shear forces contribute to a positive lift force (i.e. the two spheres repel each other) when the two spheres are close.

On the other hand, when the two spheres are in the intermediate separation regime, the velocity vector distributions show that the front stagnation streamline is almost straight, and thus the flow in the lower left region is not affected by the presence of the other sphere. Nevertheless, the gap between the two spheres causes the flow to accelerate slightly faster on the top of the sphere than on the bottom and, as a result, the average pressure in the lower region is slightly higher than that in the narrow gap. Thus, the two spheres attract each other weakly, and the attraction force is mainly due to the pressure distribution. The shear force, nearly parallel to the x-axis at the top of the sphere, contributes mainly to the drag but not to the lift.

3.2.4. *Moment and drag coefficients*

Figure 12 shows the moment coefficient as a function of dimensionless distance at Reynolds numbers 50, 100, and 150. The moment coefficient is positive when the two spheres are close ($d_0 < 4.6$ for $Re = 50$, $d_0 < 2.5$ for $Re = 100$, and $d_0 < 1.96$ for $Re = 150$), that is, the two spheres experience positive torque, and the torque becomes stronger the closer they are. On the other hand, the moment coefficient is negative at intermediate separation distances. The moment essentially vanishes, and the two spheres have negligible interactions with each other when $d_0 \geqslant 21$. In our calculations, the solid spheres were not allowed to rotate under the influence of the torque.

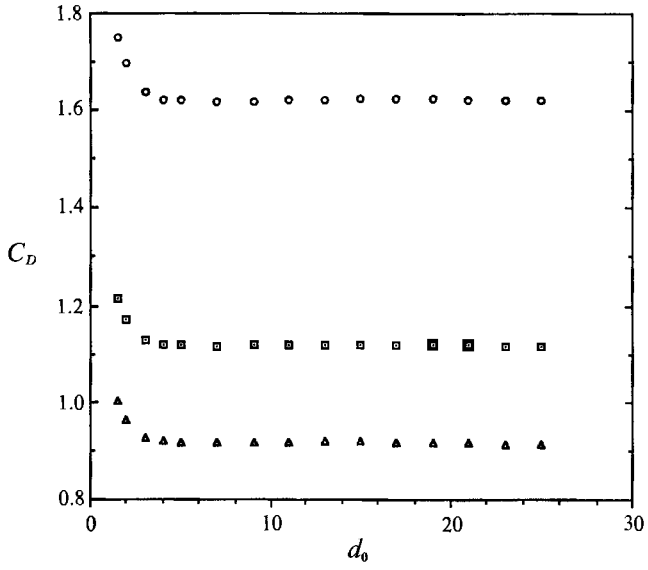

FIGURE 13. Drag coefficient of the solid spheres as a function of d_0 at $Re = 50$, 100, and 150. Symbols as figure 11.

When the two spheres are close, the shear stress, on average, is higher around the lower part of the sphere than around the top, and thus they experience positive torque. On the other hand, when the spheres are at the intermediate separation distances, slightly higher velocity in the gap leads to slightly higher shear stress on the top than on the bottom of the sphere, and this causes the spheres to experience weak negative torque.

We note that the torque acting on the sphere is relatively small, and the moment coefficient is less than 1 % of the drag coefficient for all the separation distances and Reynolds numbers. The main reason for this is that the torque depends only on the distribution of the shear stresses ($\tau_{r\theta}$ and $\tau_{r\phi}$) and, as shown in figure 9, the shear stress on the top of the sphere counteracts that on the left bottom of the sphere.

Figure 13 shows the drag coefficient as a function of the dimensionless distance at Reynolds numbers 50, 100, and 150. The drag increases with decreasing d_0 when d_0 is less than 4 for all Reynolds numbers. It increases slightly with increasing d_0 at intermediate separation distances, and eventually tends to that of a single sphere when $d_0 \geqslant 21$. The drag increases as the two spheres get close because the shear stress on the sphere is increased and the pressure distribution is changed owing to the flow acceleration on the lower left region as well as in the gap between them, as shown in figures 8 and 9.

3.3. *Interactions of two liquid spheres*

In the analysis of the flow field past two liquid spheres, we use a viscosity ratio (internal fluid to external fluid) of 25 and density ratio of 300. These values are typical of liquid-hydrocarbon fuel in a high-temperature high-pressure surrounding gas generally encountered in gas turbine combustors (Raju & Sirignano 1990).

As in the solid-sphere case, we examine the flow field for two liquid spheres in the (x, z)-plane of symmetry, the *principal plane*, where the narrowest path between the liquid spheres is encountered. Figure 5(*a–c*) discussed in §3.2.1 can also represent typical streamlines in the external flow of liquid spheres. However, there are differences from the solid-sphere case. First, the angle, measured from $\theta = 0$, at

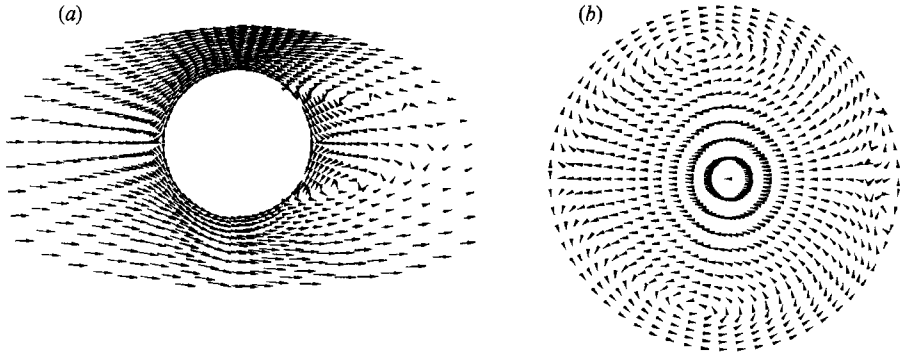

FIGURE 14. Velocity vector fields in the principal plane for a liquid sphere at $Re = 100$ for $d_0 = 2$: (*a*) external flow; (*b*) internal flow.

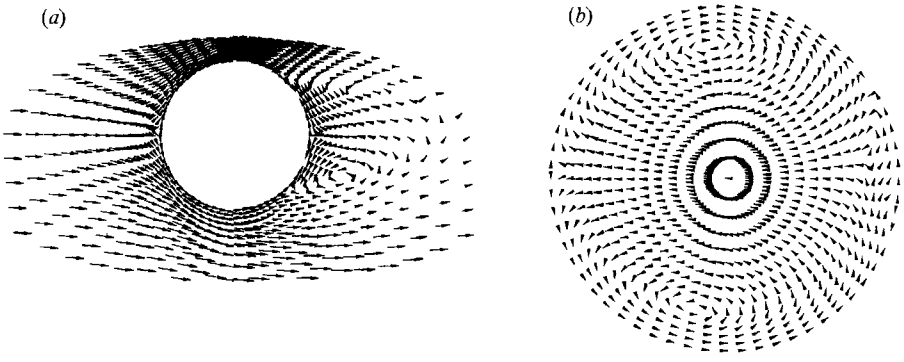

FIGURE 15. Velocity vector fields in the principal plane for a liquid sphere at $Re = 100$ for $d_0 = 1.5$: (*a*) external flow; (*b*) internal flow.

which separation occurs on the sphere surface is much higher than that of the solid sphere. Second, a closer examination of the velocity plot (figures 14*a* and 15*a*) in the wake region indicates that the separating streamline, instead of being nearly normal to the sphere surface, now curves closer to the sphere surface, producing a 'squashed' recirculation zone. This behaviour was also seen in the velocity vector field of axisymmetric flow in figure 4(*a*). The length of the recirculating eddy is also slightly smaller than that of the solid sphere.

Figure 14(*a*, *b*) shows the velocity vector fields of the external and internal flows, respectively, in the principal plane at Reynolds number 100 where the two spheres are separated by a distance $d_0 = 2$. A secondary eddy in the liquid-sphere stern region is evident in both the upper and lower regions in the principal plane, but the eddy centres in both regions are asymmetrical with respect to the $z = 0$ plane. Also, these eddies are concomitant with the occurrence of the eddies in both regions in the external flow. Figure 15(*a*, *b*) shows the velocity vector fields of the external and internal flows in the principal plane at Reynolds number 100 for the case of $d_0 = 1.5$. The secondary internal eddy in the liquid-sphere stern region exists only in the lower region, and the secondary eddy in the upper region no longer exists. The vanishing secondary internal eddy in the upper region is accompanied by the disappearance of the recirculating eddy in the upper region in the external flow.

Calculations of the lift, moment, and drag coefficients were performed for dimensionless distances from the liquid sphere centre to the symmetry plane between

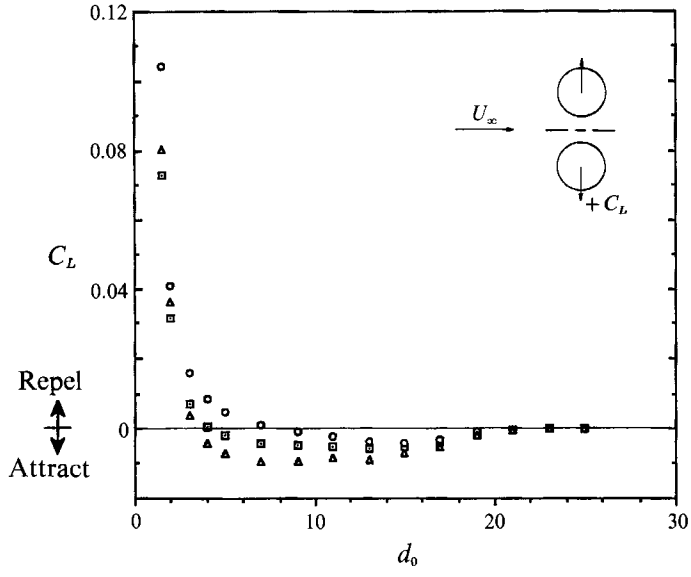

FIGURE 16. Total lift coefficient of the liquid spheres as a function of d_0 at $Re = 50$ (○), 100 (⊡), and 150 (△).

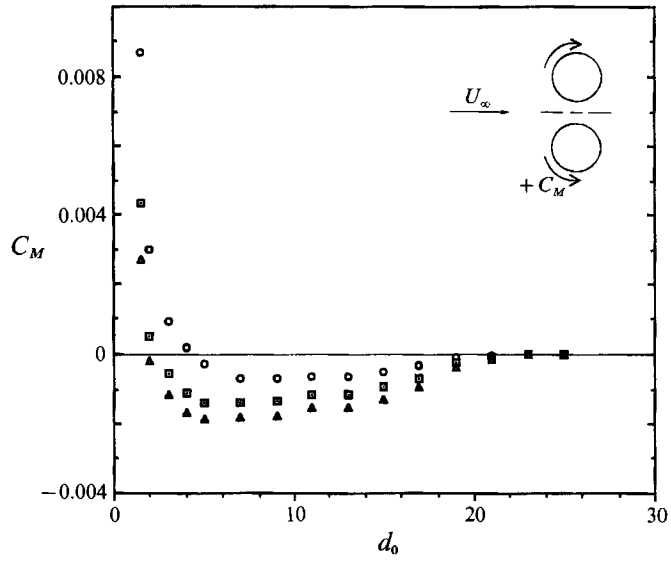

FIGURE 17. Moment coefficient of the liquid spheres as a function of d_0 at $Re = 50$, 100, and 150. Symbols as figure 16.

two liquid spheres in the range $1.5 \leqslant d_0 \leqslant 25$, for a viscosity ratio of 25 and density ratio of 300 at Reynolds numbers 50, 100, and 150. Figures 16, 17, and 18 show the coefficients of total lift, moment, and drag as a function of dimensionless distance at Reynolds numbers 50, 100, and 150. The coefficients of total lift, moment, and drag are slightly smaller in absolute value than those for the solid spheres at both the repelling and attraction separation distances and at all Reynolds numbers. The lower coefficients of the liquid sphere are attributed to the surface motion of the liquid

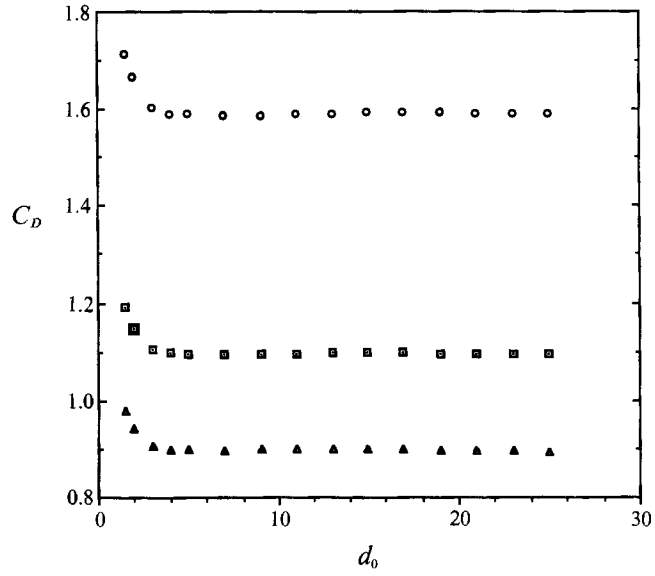

FIGURE 18. Drag coefficient of the liquid spheres as a function of d_0 at $Re = 50$, 100, and 150. Symbols as figure 16.

sphere which reduces the velocity gradient and friction force. A smaller drag coefficient for the liquid sphere in axisymmetric flow has been also found in earlier calculations (Clift *et al.* 1978).

4. Conclusions

Three-dimensional flow interactions between two identical (solid or liquid) spheres which are held fixed, with the line connecting the sphere centres normal to a uniform stream, have been investigated at Reynolds numbers 50, 100, and 150 as a first step towards understanding the three-dimensional interactions with a large concentration of particles.

First, the interactions between two solid spheres have been investigated for a dimensionless distance in the range $1.5 \leqslant d_0 \leqslant 25$.

The two spheres repel each other when they are close ($d_0 < 7.9$ for $Re = 50$, $d_0 < 4$ for $Re = 100$, and $d_0 < 3.4$ for $Re = 150$), and the repulsion is stronger the closer they are. On the other hand, the two spheres attract each other weakly at intermediate separation distances ($7.9 < d_0 < 21$ for $Re = 50$, $4 < d_0 < 21$ for $Re = 100$, and $3.4 < d_0 < 21$ for $Re = 150$). For $d_0 \geqslant 21$, however, the lift vanishes, and the two spheres do not interact at any Reynolds numbers.

The two spheres experience positive torque when they are close ($d_0 < 4.6$ for $Re = 50$, $d_0 < 2.5$ for $Re = 100$, and $d_0 < 1.96$ for $Re = 150$), and the torque is stronger the closer they are. On the other hand, the moment coefficient is negative at intermediate separation distances. The moment vanishes, and the two spheres do not interact when $d_0 \geqslant 21$. The drag on the spheres increases when d_0 is less than 4 for all Reynolds numbers. It increases slightly at intermediate separation distances, and eventually, tends to that of a single sphere when $d_0 \geqslant 21$.

The flow structure ahead of each sphere is such that the streamlines shift away from the x, y symmetry plane due to the flow *blockage* in the gap between the two spheres as they approach the front stagnation region. Also, interesting phenomena

in the near wake have been discovered as the gap between the two spheres decreases. When $d_0 = 2$, the upper eddy is not formed by the fluid separating on the upper portion of the sphere, but rather by the fluid turning around the lower eddy and detached from the sphere. Furthermore, when d_0 decreases to 1.5, both the upper eddy and downstream stagnation point vanish.

The interactions between two liquid spheres have been also investigated for the dimensionless distance in the range $1.5 \leqslant d_0 \leqslant 25$ for a viscosity ratio of 25 and density ratio of 300 at Reynolds numbers 50, 100, and 150.

The magnitudes of the lift, torque, and drag on the liquid spheres are slightly smaller in absolute value than those of the solid spheres at all the separation distances and all Reynolds numbers. The flow structure in the external flow of the liquid spheres is quite similar to that of the solid spheres, except that the separation angle is much higher than that of the solid spheres and the separation streamline is bent closer to the sphere surface producing a 'squashed' recirculation zone.

This work has been supported by the Air Force Office of Scientific Research under grant No. 90-0064 with Dr Julian Tishkoff acting as the technical monitor. We would like to thank Mr Lyle Wiedeman and Dr Allen Schiano for their assistance in using a three-dimensional graphic package Application Visualization System (AVS). The support of the Pittsburgh Supercomputing Center and the San Diego Supercomputer Center under a block grant of the Office of Academic Computing of UCI are gratefully appreciated.

REFERENCES

ANDERSON, D. A., TANNEHILL, J. C. & PLETCHER, R. H. 1984 *Computational Fluid Mechanics and Heat Transfer*. Hemisphere.

CHIANG, C. H. & SIRIGNANO, W. A. 1992*a* Numerical analysis of interacting, convecting, vaporizing fuel droplets with variable properties. *Intl J. Heat Mass Transfer* (in press).

CHIANG, C. H. & SIRIGNANO, W. A. 1992*b* Axisymmetric calculations of three-droplets interactions. *Atomization and Sprays* (in press).

CLIFT, R., GRACE, J. R. & WEBER, M. E. 1978 *Bubbles, Drops, and Particles*. Academic.

DANDY, D. S. & DWYER, H. A. 1990 A sphere in shear flow a finite Reynolds number: effect of shear on particle lift, drag, and heat transfer. *J. Fluid Mech.* **216**, 381–410.

GOLDBURG, A. & FLORSHEIM, B. H. 1966 Transition and Strouhal number for the incompressible wake of various bodies. *Phys. Fluids* **9**, 45–50.

KIM, I. & PEARLSTEIN, A. J. 1990 Stability of the flow past a sphere. *J. Fluid Mech.* **211**, 73–93.

NAKAMURA, I. 1976 Steady wake behind a sphere. *Phys. Fluids* **19**, 5–8.

PATNAIK, G. 1986 A numerical solution of droplet vaporization with convection. Ph.D. dissertation, Carnegie-Mellon University.

RAJU, M. S. & SIRIGNANO, W. A. 1990 Interaction between two vaporizing droplets in an intermediate-Reynolds-number flow. *Phys. Fluids* A **2**, 1780–1796.

RIVKIND, V. Y. & RYSKIN, G. 1976 Flow structure in motion of a spherical drop in a fluid medium at intermediate Reynolds numbers. *Fluid Dyn.* **11**, 5–12.

ROOS, F. W. & WILLMARTH, W. W. 1971 Some experimental results on sphere and disk drag. *AIAA J.* **9**, 285–291.

ROSFJORD, T. J. 1974 Experimental and theoretical investigations of the recirculating flow region between two-dimensional, parallel, separated jets. Ph.D. dissertation, Princeton University.

SIRIGNANO, W. A. 1983 Fuel droplet vaporization and spray combustion. *Prog. Energy Combust. Sci.* **9**, 291–322.

TAL(THAU), R., LEE, D. N. & SIRIGNANO, W. A. 1983 Hydrodynamics and heat transfer in sphere assemblages – cylindrical cell models. *Intl J. Heat Mass Transfer* **26**, 1265–1273.

TAL(THAU), R., LEE, D. N. & SIRIGNANO, W. A. 1984 Heat and momentum transfer around a pair of spheres in viscous flow. *Intl J. Heat Mass Transfer* **27**, 1253–1262.

TANEDA, S. 1956 Experimental investigation of the wake behind a sphere at low Reynolds number. *J. Phys. Soc. Japan* **11**, 1104–1108.

TOMBOULIDES, A. G., ORSZAG, S. A. & KARNIADAKIS, G. E. 1991 Three-dimensional simulation of flow past a sphere. *Intl Soc. Offshore Polar Engng Proc.* Edinburgh, Scotland.

VINOKUR, M. 1983 On one-dimensional stretching functions for finite-difference calculations. *J. Comput. Phys.* **50**, 215–234.